Nanoscale

PAPER

View Article Online
View Journal | View Issue

Published on 28 January 2014. Downloaded by Université Laval on 15/05/2014 20:42:49.

Cite this: *Nanoscale*, 2014, **6**, 4819

Design of multicomponent photocatalysts for hydrogen production under visible light using water-soluble titanate nanodisks†

Cao-Thang Dinh,[a] Minh-Hao Pham,[a] Yongbeom Seo,[b] Freddy Kleitz*[c] and Trong-On Do*[a]

Received 12th December 2013
Accepted 22nd January 2014

DOI: 10.1039/c3nr06602a

www.rsc.org/nanoscale

We report the design of efficient multicomponent photocatalysts (MPs) for H_2 production under visible light by using water-soluble ultrathin titanate nanodisks (TNDs) stabilized by tetraethylammonium cations (TEA^+) as building blocks. The photocatalysts are designed in such a way to significantly enhance simultaneously the efficiency of the three main steps in the photocatalytic process *i.e.*, light absorption, charge separation and catalytic reaction. We show, as an example, the construction of water-soluble CdS–TND–Ni MPs. The designed CdS–TND–Ni MPs, in which CdS nanoparticles and TNDs are intimately assembled to enhance the charge transfer and surface area, are controlled in composition to optimize visible light absorption. The conception of the MPs allows them to be highly dispersed in water which markedly improves the photocatalytic H_2 production process. Most importantly, a Ni co-catalyst is selectively located on the surface of TNDs, enabling vectorial electron transfer from CdS to TND and to Ni, which drastically improves the charge separation. Consequently, under visible light illumination ($\lambda \geq 420$ nm), the optimally designed CdS–TND–Ni MPs could generate H_2 from ethanol–water solution with rate as high as 15.326 mmol g^{-1} h^{-1} during a reaction course of 15 h and with an apparent quantum yield of 24% at 420 nm. Moreover, we also demonstrate that TNDs can be combined with other single or mixed metal sulfide to form water-soluble metal sulfide–TNDs composites which could also be of great interest for photocatalytic H_2 production.

1. Introduction

Since the discovery of photo-induced water splitting on TiO_2 electrode,[1] the use of semiconductors for photocatalytic H_2 production from water has attracted tremendous amount of interest as it enables the production of clean and renewable energy directly from solar irradiation. To date, the most challenging issue, which prevents photocatalytic H_2 production from commercial use, is to develop highly efficient photocatalysts that effectively harvest sunlight and are capable of driving the water splitting reactions.[2–7] In general, photocatalytic H_2 production is determined primarily by three reaction processes: light-harvesting; charge generation and separation; and catalytic H_2 evolution.[8–10] Thus, efficient photocatalysts for H_2 production need not only to exhibit a small bandgap with suitable flat band to strongly absorb visible light (accounting for about 43% of the solar spectrum), but also effective charge separation capability, high surface area, and good dispersion properties in the reacting medium.[8]

Due to several simultaneous requirements to achieve efficient photocatalysts, single semiconductors are usually suffering from limitations.[8,11–14] To overcome this, composite systems built of more than two semiconductor components have been considered promising because they can compensate for the disadvantages of the individual components, and induce synergistic effects, such as an efficient charge separation, strong visible light absorption, and improvement of photostability.[10–14] Among various composite photocatalysts, titanium oxide based nanocomposites in which TiO_2 or titanate materials are combined with suitable small bandgap semiconductors (SBSCs) such as metal sulfides have attracted the most attention.[15–23] Titanium oxide materials including anatase, rutile TiO_2 and titanate are generally the most widely studied photocatalysts because of their high activities, good stabilities, low costs and environmental friendliness.[15–28] Particularly, titanate materials such as titanate nanotubes and titanate nanosheets, with suitable conduction band (CB) and very high surface area, are of great interests for photocatalytic H_2 production.[19–21] When combined with suitable SBSCs, the SBSCs–titanium oxide

[a]*Department of Chemical Engineering and Centre de Catalyse et Chimie Verte, Laval University, Quebec, G1V 0A6, Canada. E-mail: trong-on.do@gch.ulaval.ca*

[b]*Department of Chemistry, KAIST and Center for Nanomaterials and Chemical Reaction, Institute for Basic Science (IBS), Daejeon 305-701, Republic of Korea*

[c]*Department of Chemistry and Centre de Recherche sur les Matériaux Avancés, Laval University, Quebec, G1V 0A6, Canada. E-mail: freddy.kleitz@chm.ulaval.ca*

† Electronic supplementary information (ESI) available: Additional characterization results. See DOI: 10.1039/c3nr06602a

Published on 28 January 2014. Downloaded by Université Laval on 15/05/2014 20:42:49.

assembly will effectively absorb visible light, and the charge injection from the CB of the SBSCs to that of the titanium oxide can lead to more efficient and longer charge separation by limiting electron–hole pair recombination, which in turn improves markedly the photocatalytic properties.[15–21]

Several SBSC–titanium oxide composite photocatalysts, *e.g.*, CdS–TiO_2 nanotubes,[15–17] CdS–TiO_2 nanowires,[18] CdS–titanate nanotubes,[19] CdS–titanate nanosheets,[20,21] have been produced using a variety of techniques including co-precipitation, photodeposition, chemical bath deposition, or layer-by-layer deposition.[15–21] Although these composites have shown improved photocatalytic activities compared to their single component counterparts, there are still several drawbacks. First of all, most of the reported SBSC–titanium oxide composites are under powder form which exhibits a relatively low dispersion in water. As photocatalytic H_2 production is performed in aqueous medium, high dispersion of the photocatalysts may sustain this process under "homogeneous-like" reaction conditions, making the photocatalytic H_2 production more efficient.[29] Second, it is still challenging to simultaneously control the composition and the interaction between the components in the composite, since an increase of the content of SBSC often tends to reduce the effective interaction between the SBSC and titanium oxide species.[30] While a high content of SBSC offers an effective visible light absorption, a less effective interaction between SBSC and titanium oxide reduces charge transfer. Third, it has been demonstrated that, adding co-catalysts, such as Pt, NiO_x nanoparticles (NPs), to the SBSC–titanium oxide composites could lead to a great improvement in photocatalytic H_2 production rates.[19,31] Here, the location of the co-catalysts in the SBSC–titanium oxide composites was however found to strongly affect the photocatalytic activity.[31] Particularly, the highest photocatalytic activity for H_2 production is obtained when the co-catalysts are located on the surface of titanium resulting in composite materials in which electrons are vectorially transferred from SBSCs to titanium oxide and then to co-catalysts.[31] Currently, the co-catalysts are essentially randomly deposited on the surface of SBSC–titanium oxide composites. There is thus no effective method available which permits a truly selective location of the co-catalysts.

We have recently reported a size-controlled synthesis of ultrathin titanate nanosheets with round shape (denoted as titanate nanodisks, TNDs).[32] These TNDs, whose negatively charged surface is compensated by tetraethylammonium cations (TEA^+), are highly dispersed in water (namely, water-soluble TNDs), and can be used for the construction of various high surface area nanostructured composites.[32] In this work, we now demonstrate the application of these water-soluble TNDs for the design of efficient multicomponent photocatalysts (MPs) suitable for photocatalytic H_2 production under visible light. We choose CdS as the SBSC and Ni as the co-catalyst, to combine with TNDs for generating CdS–TND–Ni MPs. CdS has been demonstrated as active photocatalysts for H_2 production under visible light due to its small bandgap and suitable flat-band,[33–35] while inexpensive Ni species such as metallic Ni or NiO_x have shown excellent properties as co-catalysts for H_2 evolution.[36–39] In our system, we found that, under visible light illumination ($\lambda \geq 420$ nm), the optimally designed CdS–TND–Ni MPs could generate H_2 from ethanol–water solution with rate as high as 15.326 mmol g^{-1} h^{-1} during a reaction course of 15 h with an apparent quantum yield of 24% at 420 nm, representing one of the most active metal sulfide–titanium oxide composite photocatalysts. The high activity and stability of the CdS–TND–Ni MPs for photocatalytic H_2 production originate from the use of water-soluble TNDs, stabilized by TEA cations, as building blocks. The TEA^+ on the surface of TNDs can be effectively exchanged with Cd^{2+} cations, which are then converted to CdS NPs located between TNDs in intimate contact to the TND surface. In addition, this process can be repeated to obtain CdS–TND composites with very high surface area, optimal composition and structure optimized for photocatalytic H_2 production. Furthermore, the presence of TEA^+ on the surface of TNDs allows for high dispersion of the resulting CdS–TND composites in water facilitating photocatalytic H_2 production. Finally, the TEA^+ species on the surface of TNDs in CdS–TND composites can be ion exchanged with Ni^{2+}, leading to the selective location of the Ni co-catalysts at the surface of TNDs in the CdS–TND composites which maximizes charge separation in the material.

2. Results and discussion

2.1. Synthesis of water-soluble CdS–TND composites

Our strategy to produce a new type of water-soluble CdS–TND composite consists of two steps. In the first step, TNDs were synthesized using a nonaqueous approach as reported by us previously.[32] The obtained oleylamine-stabilized TNDs were then cation-exchanged with tetraethylammonium (TEA) cations to produce TEA^+-exchanged TNDs (TEA–TND) which are soluble in water. Transmission electron microscopy (TEM) data (Fig. S1a and b†) reveal that the obtained TNDs are uniform in size with a mean particle diameter of 20 nm and a thickness of 0.75 nm. The high resolution TEM (HRTEM) image (Fig. S1c†) shows a *d*-spacing of 0.19 nm which is corresponding to the crystalline lattice of the (200) plane in the lepidocrocite-type titanate structure. The crystal structure of the TND was also confirmed by wide-angle powder X-ray diffraction (XRD) (Fig. S2†) showing the presence of a peak at 48.3° which corresponds to the interplanar distance of 0.19 nm in the TNDs.

In the second step, CdS NPs were grown between TND layers using a multi-cycle pathway as depicted in Scheme 1. Each cycle consists of (i) exchanging the TEA^+–TND with Cd^{2+} to form precipitated Cd^{2+}–TND; and (ii) reacting Cd^{2+}–TND with TEA^+ cations and thiourea at 70 °C to form a TEA^+–CdS–TND composite dispersed in water. The key point in this strategy is that, once the Cd^{2+} cations located between the TND layers are converted to CdS NPs attached to TND by reacting with S^{2-}, the negative charge of the TND surface is again compensated by TEA^+. This produces a TEA^+–CdS–TND composite which is soluble in water. Hence, the TEA^+–CdS–TND is ready for another cation exchange with Cd^{2+} starting a new cycle. As a result, by repeating this cycle, we can both increase the content of CdS and tune the morphology of the resulting composite, and consequently, composite systems with desired morphology and composition can be obtained. It is also noted that, the use of

 This journal is © The Royal Society of Chemistry 2014

Published on 28 January 2014. Downloaded by Université Laval on 15/05/2014 20:42:49.

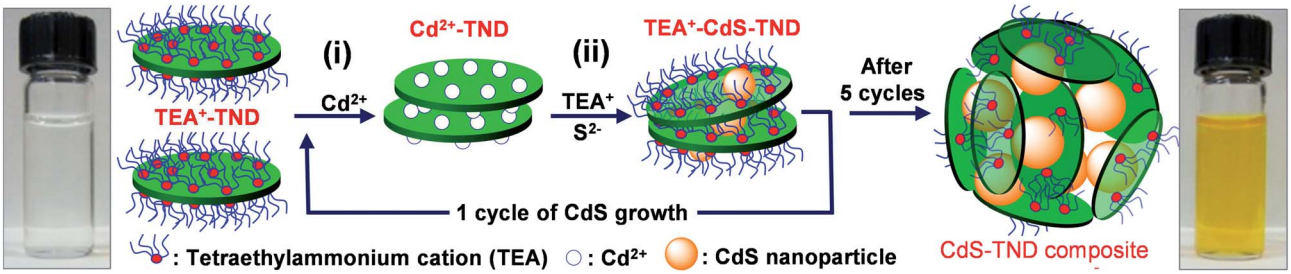

Scheme 1 Illustration of the synthesis of the water-soluble CdS–TND composite colloids. (i) Exchanging the TEA^+–TND with Cd^{2+} to form Cd^{2+}–TND; (ii) reacting Cd^{2+}–TND with TEA^+ and thiourea at 70 °C to form TEA^+–CdS–TND composites.

TND indeed prevents the agglomeration of the CdS NPs. A control experiment performed under similar conditions except for the presence of TND resulted in a CdS powder that precipitated in water. Thus, in our case, the TND species can act as effective stabilizers for the synthesis of CdS colloids.

2.2. Synthesis of water-soluble CdS–TND composites

2.2.1. Water-soluble property. Although several methods have been used for the synthesis of CdS–titanate composites,[19–21] our approach toward CdS–titanate composites is different. Here, by using water-soluble TNDs, we are able to design CdS–TND composite colloids, which are highly dispersed in water under static condition. As illustrated in Fig. 1a, the formation of CdS–TND composite colloids is evidenced by the observation of a clear Tyndall phenomenon. The presence of TEA in the CdS–TND composites, which makes them highly dispersed in water, was evidenced by FTIR analysis (see Fig. S3†). The two peaks at 2922 and 2850 cm^{-1} correspond to the asymmetric and symmetric stretching mode of the methylene groups present in the TEA, respectively, while the peak at 2985 cm^{-1} is associated with the CH_3 stretching vibration.[40] In addition, the CdS–TND solution exhibited a negative zeta potential of −46 mV (Fig. 1b), indicating a high stability of this colloidal solution. The American Society for Testing and Materials (ASTM) defines colloids with zeta potentials higher than 40 mV (negative or positive) to have "good stability".[41] This water-soluble property of CdS–TND composites is seen as an advantage as it will facilitate photocatalytic H_2 production which is usually performed in aqueous medium.

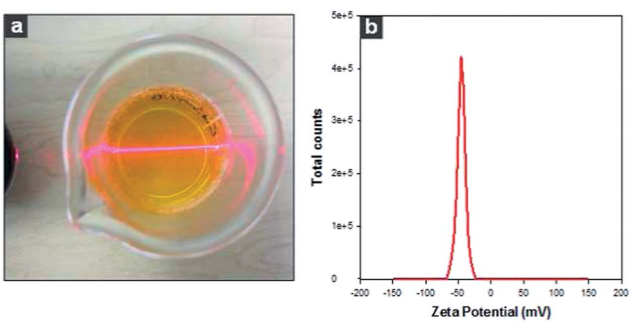

Fig. 1 Photograph of the CdS–TND solution with a typical Tyndall effect of colloidal solution (a). Zeta potential of CdS–TND composite colloidal solution measured at pH = 7.5 (b).

2.2.2. Particle morphology and crystalline structure. Fig. 2 shows TEM images of CdS–TND composites obtained with different cycles of CdS growth. It can be seen that, when the CdS growth cycle was increased from 1 to 5, the size of the resulting composites gradually increased from around 20 to 40 nm (Fig. 2a–e). When the cycle was repeated 6 times, a chain-like CdS–TND composite was obtained (Fig. 2f). The crystallographic structure of CdS in the composites is revealed by X-ray diffraction. Fig. 2g shows the XRD pattern of the resulting CdS–TND composites obtained with different number of CdS growth cycles. It is seen that all of the diffraction peaks of the CdS in the composites could be indexed either as cubic CdS (JSPDS Card no. 10-0454) or as hexagonal CdS (JSPDS Card no. 41-1049). The peaks at 26.5°, 44.0°, and 52.1° correspond to the diffractions of the (111), (220), and (311) planes of cubic CdS, respectively. The presence of two shoulder peaks located at 2-theta of 25.02° and 28.02° suggests the occurrence of hexagonal CdS in the obtained CdS–TND composite colloids. The diffraction peaks are broad because the crystallite sizes of CdS NPs in the samples are relatively small. Also observed in the XRD patterns of the CdS–TND composites is a diffraction peak at 2-theta of 48.30° which corresponds to the (200) plane of the TNDs. No additional peak attributed to a titanium dioxide phase was observed from the XRD patterns suggesting that the titanate phase was maintained after six CdS growth cycles.

The morphology and structure of the CdS–TND composites were further characterized by TEM and HRTEM. Fig. 3 shows high magnification TEM and HRTEM images of the CdS–TND composites obtained upon 5 cycles of CdS growth. The resulting colloidal composites are uniform in size with a mean particle diameter of 40 nm, and each colloid consists of both TND and CdS NPs (Fig. 3a and b). As seen in Fig. 2b and c, the TNDs and CdS NPs are mutually intercalated forming composite colloids with multipoint contacts at the interface between the two nanodomains. High magnification HRTEM images taken from different areas of a composite colloid show the details of the crystallite phase of both titanate and CdS compositions. As seen in Fig. 3d, the lattice fringe with *d*-spacing of 0.19 nm corresponds to the (200) of TND. Fig. 3e shows a lattice fringe with *d*-spacing of 0.336 nm which can be assigned to the (111) lattice plane of the cubic CdS. The existence of hexagonal CdS was further corroborated by the presence of two lattice fringes with

Published on 28 January 2014. Downloaded by Université Laval on 15/05/2014 20:42:49.

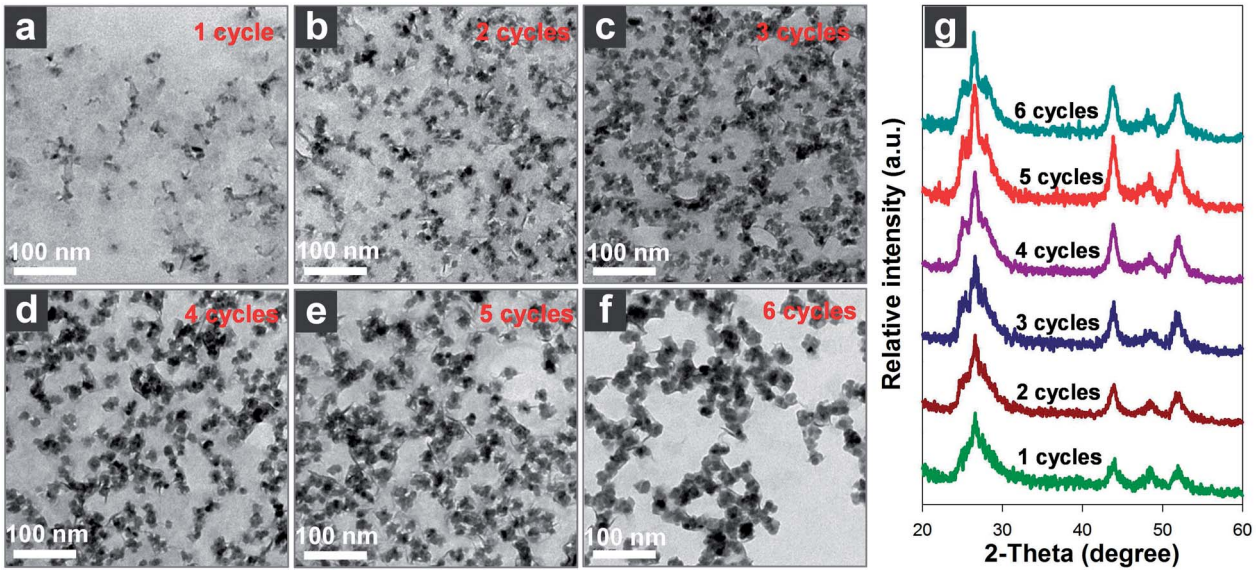

Fig. 2 TEM images (a–f) and XRD patterns (g) of the CdS–TND composites obtained at different stages of the growth process.

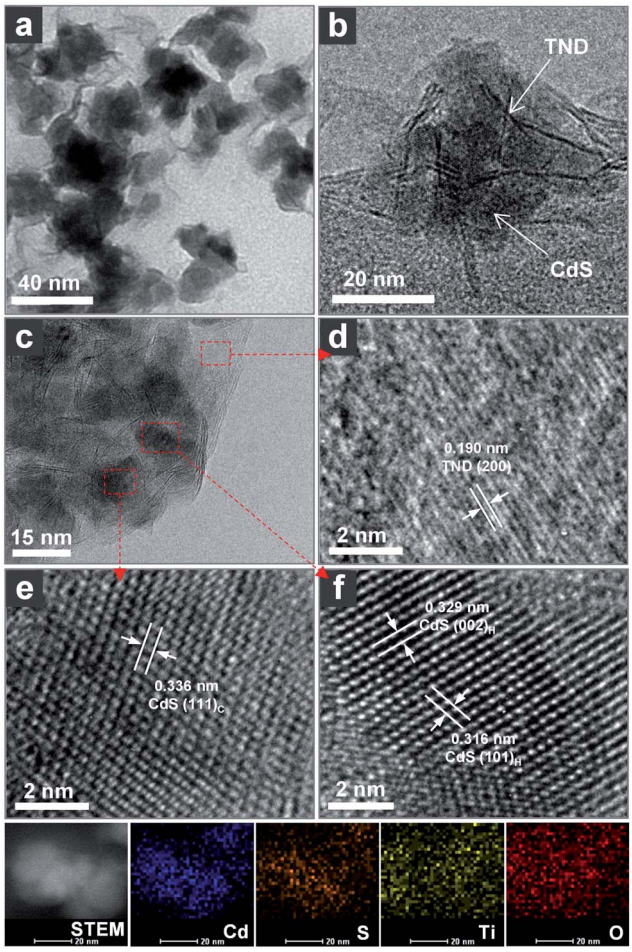

Fig. 3 TEM (a and b), HRTEM (c–f) images and EDX elemental mapping data (lower panel) of the CdS–TND composite obtained by 5 cycles of CdS growth.

interlayer distance of 0.329 and 0.316 nm which correspond to the lattice spacing of the (002) and (101) planes in the hexagonal CdS (Fig. 3f). Elemental mapping of an individual CdS–TND composite colloid particle is depicted in Fig. 3 (lower panel). These analyses clearly demonstrate homogeneous distribution of Cd, S, Ti, and O elements over the composite. This result further confirms that TND and CdS NPs are uniformly intercalated together in the colloidal composite structure.

2.2.3. Composition, optical properties and porous structure. The composition of the CdS–TND composites was determined using EDX technique as shown in Fig. 4a. It can be observed that, the Cd : Ti molar ratio increases almost linearly with increasing growth cycle indicating that a similar amount of CdS was introduced after each of the cycles. After 5 cycles of CdS growth, a Cd : Ti molar ratio of 1.14 is measured in the obtained composite. Thermogravimetric analysis (TGA) of this sample reveals 8.0 wt% of TEA present in the CdS–TND composites (Fig. S4†). Fig. 4b shows the diffuse-reflectance UV-vis spectra of the CdS–TND composites, in comparison to the TEA–TNDs. It can be observed that, the TNDs only adsorb the light with wavelength lower than 320 nm owing to their large band-gap of 3.8 eV. In contrast, the CdS–TNDs composites exhibited light absorption in both ultraviolet and visible regions. The absorption intensity at around 480 nm, which corresponds to the presence of the CdS domain, increases with more CdS growth cycles, in line with an increasing CdS content after each CdS growth cycle.

The porous structure of the CdS–TND composite obtained by 5 cycles of CdS growth was characterized using N_2 adsorption–desorption at −196 °C. Prior to performing this analysis, the TEA on the surface of the composite was exchanged with H^+ by treating the CdS–TND composite with dilute HNO_3 solution to avoid the effect of TEA during the analysis. As shown in Fig. 4c, the N_2 sorption isotherm of the CdS–TND composite corresponds to type-IV isotherm with a H2 hysteresis loop

 This journal is © The Royal Society of Chemistry 2014

Published on 28 January 2014. Downloaded by Université Laval on 15/05/2014 20:42:49.

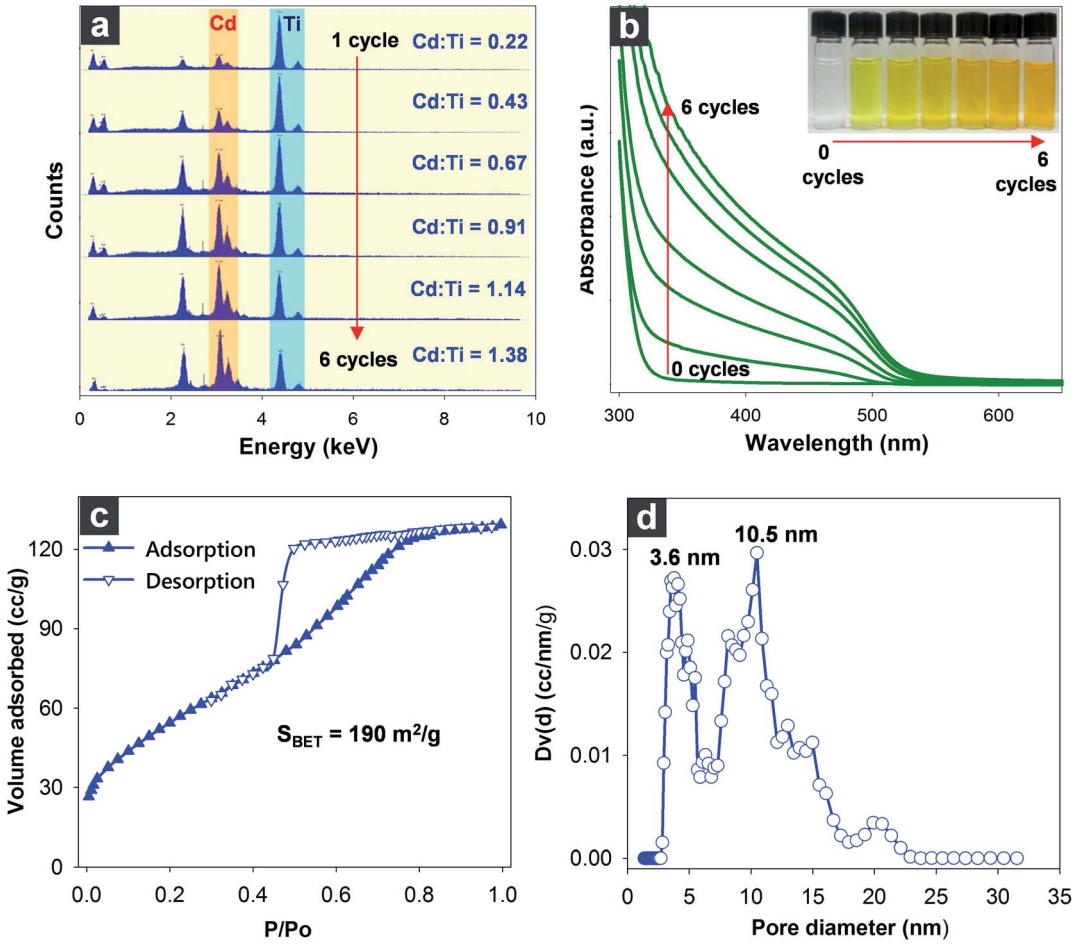

Fig. 4 EDX (a) and UV-vis spectra (b), photographs (inset in b) of the CdS–TND composites obtained at different stages of the CdS growth process. Nitrogen sorption isotherms (c) measured at −196 °C for CdS–TND composites, obtained by 5 cycles of CdS growth, after the treatment with dilute HNO_3 to replace the TEA cations with H^+ and the respective NLDFT pore size distribution calculated from the adsorption branch (d).

characteristic of mesoporous materials with large cage-like or ink-bottle type pores.[42] The pore size distribution calculated applying the nonlocal density functional theory (NLDFT) method on the adsorption branch (Fig. 4d), reveals two main maxima, at about 3.6 nm and 10.5 nm, which may be originating from two populations of inter-particulate voids both inside and between the CdS–TND colloidal composite particles. The specific surface area of this composite as calculated using the standard BET method reaches 190 $m^2\ g^{-1}$. It should be noted that, the specific surface area of bare TND and CdS synthesized in similar conditions were only of 35 and 26 $m^2\ g^{-1}$, respectively. This indicates that, the combination of TND and CdS using the present approach substantially improves the surface area of these materials.

2.3. Photocatalytic H_2 production activity of CdS–TND composites using Ni co-catalysts

Photocatalytic H_2 production activities of the samples were evaluated under visible-light irradiation using ethanol as a sacrificial reagent and Ni as a co-catalyst. The ethanol can prevent sulfide photocatalysts from the photocorrosion by providing sacrificial electron donors to consume the photogenerated holes, and Ni can decrease the overpotential in the production of H_2 from water.

Fig. 5a shows the photocatalytic H_2 production rates of CdS–TND composites obtained with different CdS-growth cycles, denoted as C_x, where x is the number of CdS-growth cycle. For comparison, photocatalytic activities of CdS alone with or without the nickel co-catalyst and that of C_5 sample without nickel co-catalyst (C_5^*) were also evaluated. The amount of Ni co-catalyst was kept at 2.8 wt% for all of the samples. As seen in Fig. 5a, all of the CdS–TND composites (C_1–C_6) exhibited higher H_2 production rate compared to CdS alone although the CdS content in the CdS–TND composites (from 28.3 wt% to 71.3 wt %) are much lower than that in CdS alone (100%). It should be noted that, TNDs alone did not produce H_2 under visible light illumination, as TNDs do not absorb visible light. When comparing the CdS–TND composites, increasing the number of CdS growth cycles clearly led to improvement in the H_2 production rate, which may be attributed to in the higher CdS content in the resulting composites. The increase of CdS content in CdS–TND composites with increasing the number of CdS growth cycles leads to a small decrease in surface area

Published on 28 January 2014. Downloaded by Université Laval on 15/05/2014 20:42:49.

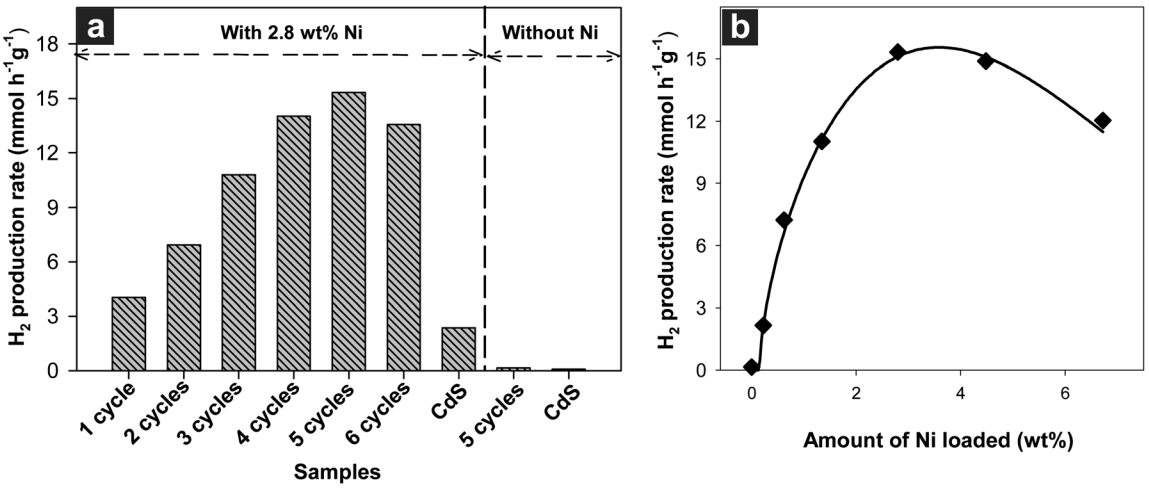

Fig. 5 (a) Comparison of the activity of different photocatalysts in the photocatalytic production of H_2 from ethanol–water mixture under visible light illumination, with or without Ni co-catalyst. (b) The rate of H_2 production on CdS–TND composites obtained through 5 cycles of CdS growth (C_5) loaded with different amounts of Ni under visible light. Reaction conditions: 20 mg of catalyst; 20 vol% ethanol solution (70 mL); light source is a xenon lamp (300 W) with a cutoff filter (λ > 420 nm).

(from 225 $m^2\ g^{-1}$ of CdS–TND with 1 CdS growth cycle to 190 $m^2\ g^{-1}$ of CdS–TND with 5 CdS growth cycles), but significantly enhances the visible light absorption of the CdS–TND composites. With five CdS growth cycles, the CdS–TND composites (C_5) show the highest H_2 production rate, *i.e.*, 15.326 mmol $g^{-1}\ h^{-1}$, which is significantly greater than that of most CdS–titanium oxide photocatalysts.[8,43] The quantum yield was estimated to be 24% at 420 nm. However, a further increase in the number of CdS growth cycle resulted in the deterioration of the catalytic performance, perhaps because the amount of TNDs in the composite was no longer sufficient to separate electrons from the CdS nanoparticles.

Obviously, the nickel co-catalyst plays here a crucial role in the photocatalytic H_2 production. Without Ni co-catalyst, the CdS sample showed a very low photocatalytic activity (0.092 mmol $g^{-1}\ h^{-1}$), which may arise from the rapid recombination of CB electrons and valence band (VB) holes and the lack of H_2 evolution sites. The CdS–TND composite with 5 CdS growth cycles (C_5), which exhibited the highest photocatalytic activity among CdS–TNDs, also showed lower H_2 production rate (0.145 mmol $g^{-1}\ h^{-1}$) without Ni co-catalysts (Fig. 5a). As shown in Fig. 5b, after loading only 0.22 wt% of Ni on CdS–TND composites (sample C_5), the activity in H_2 evolution increased by up to 15 times. With higher amounts of Ni loaded in CdS–TND composites, the rate of H_2 evolution on MPs further increased and reached a maximum with ~2.8 wt% of Ni (Fig. 5b). A further increase in the amount of the co-catalyst provoked a slight reduction of the activity which may be attributed to the precipitation of the MPs caused by the excess amount of Ni^{2+} cations on the TNDs surface.

It is important to note that metal sulfide photocatalysts are usually unstable during photocatalytic reaction due to: (i) reduction of metal cations in metal sulfides by generated electrons; (ii) oxidation of S^{2-} by generated holes; and (iii) detachment of metallic NP co-catalysts from the metal sulfide surface due to photooxidation of the metal particles.[44–46] The stability of CdS–TND–Ni MPs obtained upon 5 cycles of CdS growth, using 2.8 wt% of Ni, was studied by performing recycling experiments under the same conditions in comparison to a CdS–Ni sample. As depicted in Fig. S5,† the photocatalytic H_2 production rate of the CdS–Ni photocatalyst decreased gradually after 5 cycles and remained at only 48% of the initial rate. In contrast, the CdS–TND–Ni MPs showed no loss of photocatalytic activity, indicative of the high stability of this photocatalyst for the H_2 production. Moreover, we observed that the CdS–TND–Ni photocatalyst was still highly dispersed in the solution even after the 5 cycles of photocatalytic reaction.

Although there are numerous reports about CdS–titanate composite photocatalysts with different nanostructures and interesting photocatalytic activities under visible light irradiation, the obtained H_2 production rate in these studies were still relatively low, either with or without using Pt co-catalysts.[8,19–21,43] For example, Zhang *et al.*[21] reported a three-dimensional CdS–titanate composite nanomaterials, in which CdS NPs are spatially distributed and fixed on the surface of titanate structures. This photocatalyst generated H_2 with a rate of *ca.* 0.075 mmol $g^{-1}\ h^{-1}$ under visible light illumination using Na_2S + Na_2SO_3 as sacrificial agent and Pt as co-catalyst. In another study, Chen *et al.*[19] reported that the H_2 gas evolved at a rate of *ca.* 1.75 mmol $g^{-1}\ h^{-1}$ over a sample of CdS–titanate nanotubes in which the CdS NPs were enwrapped by the surrounding titanate nanotubes using Pt co-catalyst. Kim *et al.*[20] reported the synthesis of a CdS–titanate nanosheet composite using preformed CdS nanoparticles. Under visible light illumination, this photocatalyst generated H_2 with a rate of 1 mmol $g^{-1}\ h^{-1}$ in absence of Pt co-catalyst. In our case, the optimal design of the CdS–TND–Ni MPs offers a very high photocatalytic H_2 production rate (15.326 mmol $g^{-1}\ h^{-1}$), which is significantly higher than those of most of CdS–titanium oxide composite photocatalysts developed so far.[8,43] This result clearly highlights the

 This journal is © The Royal Society of Chemistry 2014

Published on 28 January 2014. Downloaded by Université Laval on 15/05/2014 20:42:49.

advantages of using water-soluble TNDs as starting materials for the design of MPs.

2.4. Role of Ni co-catalysts and proposed photocatalytic mechanism

The Ni co-catalyst is found to play a crucial part in designing efficient MPs. To identify the role of Ni, XPS was used to monitor the change in chemical states of Ni^{2+} after photoreduction. Fig. 6a shows the high-resolution XPS spectrum of Ni 2p in the case of the CdS–TND–Ni nanocrystals (NCs) in comparison to that of reference samples, *e.g.*, CdS–Ni and metallic Ni NPs prepared by chemical reduction using $NaBH_4$. As seen in Fig. 6a, the Ni $2p_{3/2}$ XPS spectrum of the metallic Ni NPs shows two peaks at 852.4 and 855.3 eV, corresponding to the presence of metallic Ni and NiO, respectively.[47,48] The presence of NiO in the reference sample could be due to the partial oxidation of metallic Ni NP surface upon contact with air. Similar peaks at 852.4 and 855.3 eV was also observed in the Ni 2p XPS spectrum of CdS–Ni sample, indicating the presence of both metallic Ni and NiO in the sample. Surprisingly, the XPS spectrum of Ni $2p_{3/2}$ of the CdS–TND–Ni MPs sample exhibits only one peak at binding energy of 855.3 eV, which is characteristic of NiO. The absence of metallic Ni in the CdS–TND–Ni sample could be due to the instability of metallic Ni clusters in air. Due to the strong electrostatic interaction between Ni^{2+} and TNDs, reduction of Ni^{2+} on the TNDs surface may result in ultrasmall metallic Ni clusters which are then easily oxidized upon contact with air yielding NiO.

Although adding the Ni co-catalyst enhanced the photocatalytic activity of both CdS and CdS–TND composites, the enhancement process in these two samples seems different. As observed in Fig. 5a, with Ni as a co-catalyst, CdS–Ni exhibits a 26-fold higher photocatalytic activity compared to that of CdS alone. However, in the presence of the Ni clusters, CdS–TND–Ni MPs shows a significantly increased photocatalytic activity, by a factor of 105, as compared to CdS–TND composites. To understand the effect of Ni co-catalyst on CdS and CdS–TND, we have therefore studied the reduction of Ni^{2+} both on the CdS and on CdS–TND composites (C_5) by measuring the amount of H_2 gas evolved during the reduction process. We have found that the reduction of Ni^{2+} on CdS was quite fast based on the fact that a constant H_2 evolution rate, pointing to a complete reduction of Ni^{2+}, was obtained after 15 minutes of reduction (Fig. 6a). In contrast, a constant H_2 evolution rate was only seen after 2 hours of reduction in the case of the CdS–TND composites (Fig. 6b). This observation indicates that, the reduction of Ni^{2+} on CdS is much faster than on the CdS–TND composites, which is not expected considering the higher dispersion of CdS–TND composites in the reacting medium, as compared to CdS NPs (higher dispersion would be expected to accelerate the reduction of Ni^{2+} on CdS–TNDs). To explain this, one may speculate that the reduction of Ni^{2+} in the CdS–TND composites would occur on the surface of TNDs unlike the reduction of Ni^{2+} in the CdS NP system which occurs on the surface of the CdS NPs. In the case of CdS–TND composites, under visible light illumination, the electron from CB of CdS can transfer to that of TNDs and then reduce Ni^{2+} species adsorbed on the surface of TNDs through electrostatic interactions (Fig. 7a). Due to the CB of TNDs (−0.38 V *vs.* SHE) is less negative than that of CdS (−0.7 V *vs.* SHE),[49–51] the reduction of Ni^{2+} on the surface of TNDs is therefore slower than that on the surface of CdS.

Based on these results, the high photocatalytic activity and stability of CdS–TND composites using nickel co-catalyst can be explained as follows: under visible light irradiation, the generated electrons from the CB of CdS can effectively be injected into the CB of TNDs due to an intimate interaction between the two semiconductors (see scheme in Fig. 7). Ni clusters deposited on the surface of TNDs receive the electrons from TNDs and act as active sites for the H_2 evolution. Thus, the electrons and holes in the NCs are separated from each other over three different components, leading to effective prolongation of the charge carrier lifetime and

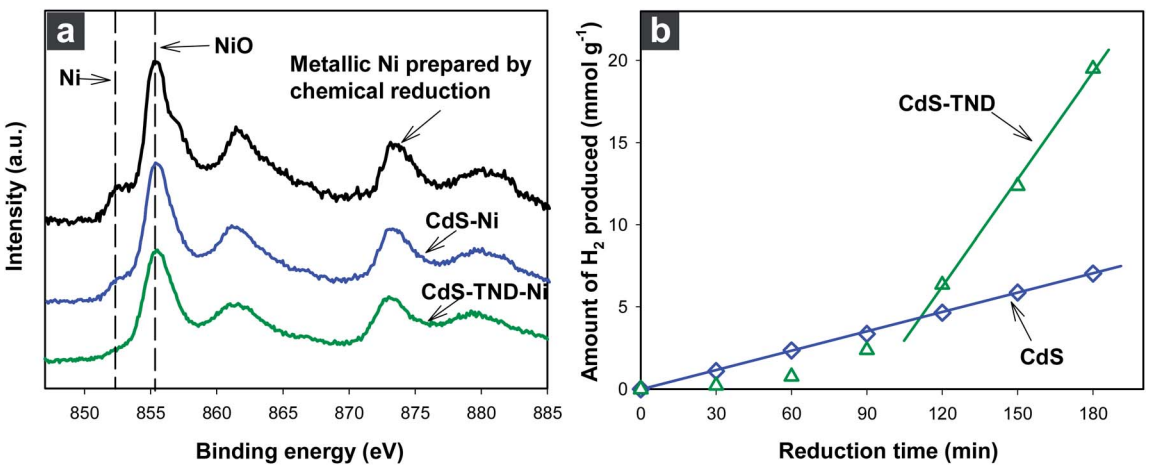

Fig. 6 XPS spectrum of Ni 2p in the CdS–TND–Ni MPs after 2 hours of Ni^{2+} reduction in comparison to that of Ni in the CdS–Ni sample and metallic Ni nanoparticles prepared by chemical reduction using $NaBH_4$ as reducing agent and $Ni(NO_3)_2$ as nickel precursor (a). Amount of H_2 gas produced as a function of irradiation time during the photoreduction of Ni^{2+} over the CdS–TND composite (sample C_5) and CdS.

Published on 28 January 2014. Downloaded by Université Laval on 15/05/2014 20:42:49.

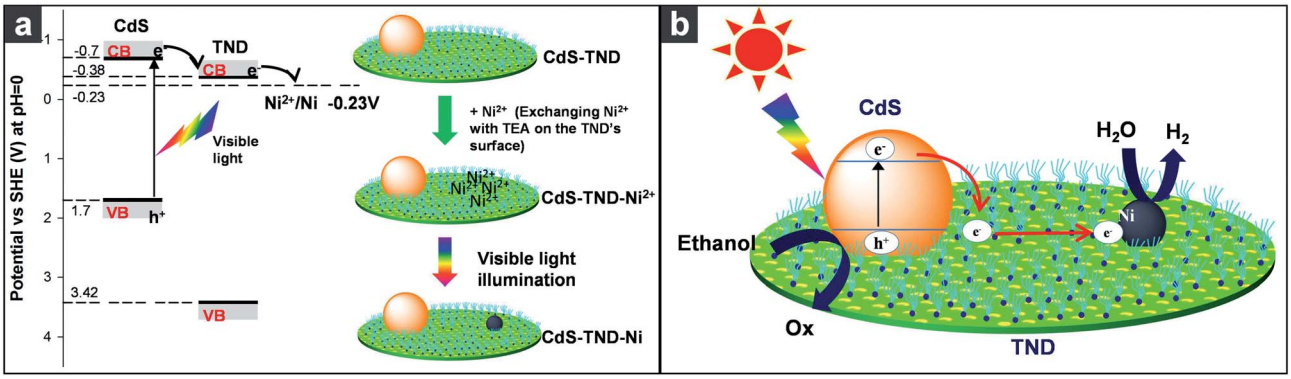

Fig. 7 Schematic illustration of the electron transfer in the photoreduction of Ni^{2+} adsorbed on the surface of TNDs under visible light illumination and schematic illustration of the formation of Ni clusters on the surface of TND in the CdS–TND composites by visible light illumination (a). Schematic illustration of the charge transfer in CdS–TND–Ni MPs in the photocatalytic H_2 production from water–ethanol mixture under visible light. To simplify, only one particle of each component is shown, although a MP colloid is composed of several CdS NPs, TNDs and Ni clusters.

enhancement of the reaction space, and consequently, the improvement of the photocatalytic H_2 production. In addition, the presence of TEA on the surface of TNDs allows excellent dispersion of the NCs in the ethanol–water mixture, but does not affect the surface of the CdS NPs and Ni clusters. Thus, the reactants (water and ethanol) may freely access the active sites both on CdS and Ni surfaces with high diffusion rate, ultimately enhancing significantly the photocatalytic rate.

One other aspect that could be considered in the case of CdS–TND–Ni MPs is the adequate electron transfer from the CB of CdS to that of TND, permitted by the intimate interactions between CdS and TND particles, which is beneficial for preventing the reduction of Cd^{2+}. In addition, the high dispersion of the photocatalysts in the reacting medium is favorable for the accessibility of sacrificial agent (ethanol) to the surface of CdS, leading to the suppression of the oxidation of S^{2-} on CdS. Furthermore, in the CdS–TND–Ni NCs, only CdS can generate holes in the VB under visible light illumination. These holes in the VB of CdS (+1.7 V *vs.* SHE) cannot be transferred to the VB of TND (+3.4 V *vs.* SHE).[49,51] Thus, Ni clusters are unlikely to be directly oxidized by holes on CdS NPs as the clusters are only located on the surface of TNDs. Taking into account these unique features, it is not surprising that the CdS–TND–Ni NCs exhibit not only high activity, but also a high stability in the photocatalytic production of H_2.

2.5. Synthesis of other water-soluble metal sulfide–TND composites

Metal sulfides have been intensively studied in photocatalysis and photovoltaic cells owing to their suitable bandgap and catalytic functions.[43] For examples, CuS–ZnS and $Cd_xZn_{1-x}S$ were demonstrated as efficient photocatalysts for water splitting.[46,52] Thus, coupling these metal sulfides with TNDs to generate composite colloids showing enhanced charge separation and combining selective location of co-catalysts can greatly improve their photocatalytic performances. Our approach can also be applied for the preparation of other water-soluble TND-based metal sulfide composites such as CuS–TNDs or ZnS–TNDs. Moreover, it is also suitable for the preparation of multicomponent composites such as ZnS–CdS–TND. To illustrate this, Fig. 8 shows that such composite colloids exhibit a size of 30–60 nm. The UV-vis results (Fig. 8d) confirm the presence of the metal sulfide phase in resulting composites as it shows typical UV-vis spectra of these semiconductor NPs.

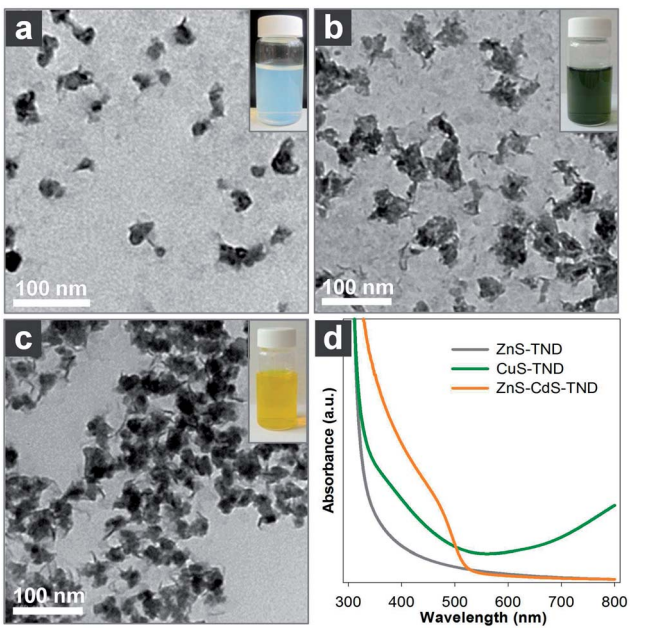

Fig. 8 (a) TEM images of: ZnS–TND composites obtained by 3 cycles of ZnS growth. (b) CuS–TND composite obtained by 4 cycles of CuS growth. (c) ZnS–CdS–TND composite obtained by 3 cycles of CdS growth and 2 cycles of ZnS growth. (d) UV-vis spectra of different metal sulfide–TND composites insets in (a–c) are photograph of the corresponding metal sulfide–TND composite solutions.

This journal is © The Royal Society of Chemistry 2014

Published on 28 January 2014. Downloaded by Université Laval on 15/05/2014 20:42:49.

3. Conclusions

In summary, we have introduced the application of water-soluble TNDs as versatile building units for assembling highly efficient MPs for H_2 production under visible light. The MPs are designed in such a way to enable a simultaneously control over: (i) the composition of the MPs with intimate interactions between the components to enhance visible light absorption and charge separation; (ii) the dispersion of high surface area MPs in water to facilitate the catalytic reaction on the surface of MPs; (iii) the relative position of the co-catalysts to maximize charge separation in the MPs through vectorial electron transfer. As an example, the optimally designed CdS–TND–Ni MPs exhibited a very high H_2 production rate of 15.326 mmol g^{-1} h^{-1} under visible light illumination and a quantum yield of 24% at 420 nm which is much higher than most of CdS–titanium oxide composites developed so far. We also demonstrated that, TNDs can be combined with other single or mixed metal sulfides forming water-soluble metal sulfide–TNDs composites which could be of great interest for photocatalytic H_2 production. We believe that, the principle introduced here, which is using water-soluble TNDs stabilized by tetraammonium cations as building blocks to construct MPs, is transferable to a wide range of other water-soluble metal oxide nanosheets.

4. Experimental section

Chemicals

All chemicals were used as received; titanium butoxide (TB), benzyl alcohol (BA), oleylamine (OM), benzyl ether, tetraethylammonium (TEA) hydroxide, copper nitrate, cadmium nitrate, zinc nitrate, acid nitric, and thiourea were purchased form Aldrich. Absolute ethanol, acetone, and toluene solvents were of analytical grade and were also purchased form Aldrich.

Synthesis of titanate nanodisks

In a typical synthesis, 2 g of TB, 12 g of OM, 12 g of BA (OM : BA weight ratio of 1 : 1), and 30 g of benzyl ether were added to a 100 mL round-bottom flask. The reaction mixture was heated to 190 °C at the heating rate 5 °C min^{-1} under nitrogen flow. After 20 h, the reaction was stopped and cooled down to room temperature. After addition of excess absolute ethanol, the TNDs were obtained by centrifugation and redispersed in toluene for microscopy analysis. The obtained nanodisks were then re-dispersed in toluene and re-precipitated with ethanol. This process was repeated three times to remove the un-reacted reagents.

Tetraethylammonium-exchanged titanate nanodisks

The as-synthesized TNDs were treated with tetraethylammonium hydroxide to obtain TEA–TNDs. Typically, 5 mmol of as-synthesized TNDs (according to Ti atom) were dispersed in a mixture of TEAOH (15 mmol), ethanol (15 mL) and water (15 mL). The mixture was stirred overnight at room temperature. An excess of acetone was added to the obtained clear solution to precipitate TNDs. The precipitate was then washed several times with acetone and finally dispersed in 10 mL of water.

Synthesis of CdS–TND and other metal sulfide–TND composites

The CdS–TND composite was synthesized using a multi-cycle pathway. In the first cycle, Cd^{2+} cations-exchanged TNDs were prepared. Accordingly, the TEA–TNDs dispersed in water were gradually added to a solution containing Cd^{2+} cations (Cd : Ti atomic ratio of 1 : 2) under stirring. The resulting Cd^{2+}–TND precipitate was then washed several times with water to remove un-exchanged Cd^{2+} cations. To obtain the CdS–TND composite, Cd^{2+}–TNDs was then dispersed in water. To this mixture was added a solution containing both TEAOH and thiourea (TEAOH : thiourea : Cd^{2+} molar ratio of 1 : 1 : 0.3). Next, the obtained mixture was heated to 70 °C. At this temperature, S^{2-} ions are released by the alkaline hydrolysis of thiourea and reacted with Cd^{2+} yielding CdS NPs. After 1 hours of heating, a yellow transparent solution was formed indicative of the formation of the CdS–TND composites. To this clear solution acetone was added in excess to precipitate CdS–TNDs. The yellow precipitate was then washed several times with acetone and finally re-dispersed in water for a subsequent CdS growth cycle. To start the second CdS growth cycle, the CdS–TND composite obtained in the previous cycle was used as precursor instead of TEA–TNDs. The following steps were similar to those of the previous cycle. This CdS growth cycle was repeated 5 times to obtain the final CdS–TND composite colloids. The synthesis of other metal sulfide–TND composites was similar to that of CdS–TND composites except other metal cations such as Cu^{2+}, Zn^{2+} were used instead of Cd^{2+}.

Synthesis of CdS NPs and CdS–Ni composite

Pure CdS NPs were prepared in the similar conditions to those of the CdS–TND composites, but in the absence of TNDs. A mixture of TEAOH and thiourea was added to the solution containing Cd^{2+} cations. The mixture was then heated to 70 °C for 1 hour. The resulting precipitate was then washed several times with water and dried at 70 °C for 5 hours. The CdS–Ni composite was also prepared for characterization using photo-deposition technique (see photocatalytic test part).

Characterization

Transmission electron microscopy (TEM) images of the samples were obtained on a JEOL JEM 1230 operated at 120 kV. High resolution TEM (HRTEM) images were performed on Philips G2 F30 Tecnai instrument operated at 300 kV. Powder X-ray diffraction (XRD) patterns of the samples were obtained on a Bruker SMART APEXII X-ray diffractometer equipped with a Cu Kα radiation source (λ = 1.5418 Å). Thermal analyses of the samples were carried out at a heating rate of 10 °C min^{-1} under a nitrogen flow up to 700 °C using a Perkin-Elmer TGA thermogravimetric analyzer. Zeta potential measurements were performed with a Zetasizer Nano ZS in water at 25 °C. X-ray photoelectron spectroscopy (XPS) measurements carried out in an ion-pumped chamber (evacuated to 10^{-9} Torr) of a

Published on 28 January 2014. Downloaded by Université Laval on 15/05/2014 20:42:49.

photoelectron spectrometer (Kratos Axis-Ultra) equipped with a focused X-ray source (Al Kα, $h\nu = 1486.6$ eV). The UV-vis spectra were recorded on a Cary 300 Bio UV-visible spectrophotometer. Fourier transform infrared (FTIR) absorption spectra were measured with a FTS 45 infrared spectrophotometer with the KBr pellet technique. N_2 adsorption–desorption isotherms of the samples were measured at −196 °C using Quantachrome Autosorb-1 MP analyzer. Before the measurements, the samples were outgassed under vacuum for 6 h at 110 °C.

Photocatalytic testing

The photocatalytic reactions were carried out in a gas-tight 200 mL Pyrex reaction cell at ambient temperature and atmospheric pressure under visible light illumination. In a typical photocatalytic experiment, 20 mg of photocatalysts were dispersed in 70 mL of aqueous solution containing 20% (v/v) of ethanol. The $Ni(NO_3)_2$ or H_2PtCl_6 solution were then added. The mixture was evacuated and purged with nitrogen for 30 minutes to remove dissolved oxygen. Then, it was illuminated with a 300 W Xe arc lamp equipped with an UV-cutoff filter (≥420 nm) for 2 hours to reduce Ni^{2+} and $PtCl_6^{2-}$ under stirring condition. The mixture was purged with nitrogen again to remove the generated H_2 during the reduction. The photocatalytic H_2 production measurements were then carried out under the same illumination condition. A 0.5 mL of gas was sampled intermittently through the septum, and hydrogen was analyzed by gas chromatography equipped with TCD detector and carboxen-1010 capillary column. The apparent quantum yield (QY) was measured under the same photocatalytic reaction conditions. The photon flux was measured with Newport's power meter equipped with a thermopile optical detector. The QY was calculated according to following equation:

$$\mathrm{QY}\ (\%) = \frac{\text{Number of reacted electron}}{\text{Number of incident photons}} \times 100$$

$$= \frac{\text{Number of evolved } H_2 \text{ molecules} \times 2}{\text{Number of incident photons}} \times 100$$

Acknowledgements

This work was supported by the Natural Sciences and Engineering Research Council of Canada (NSERC). C.T.D. thanks the FQRNT for the Excellence Scholarship. Y.S. acknowledges support from Institute for Basic Science (IBS). The authors wish to thank Prof. Ryong Ryoo (KAIST, Korea) for the access to high-resolution TEM microscope.

Notes and references

1 A. Fujishima and K. Honda, *Nature*, 1972, **238**, 37.
2 X. Chen, L. Liu, P. Y. Yu and S. S. Mao, *Science*, 2011, **331**, 746.
3 K. Maeda, K. Teramura, D. Lu, T. Takata, N. Saito, Y. Inoue and K. Domen, *Nature*, 2006, **440**, 295.
4 Z. Han, F. Qiu, R. Eisenberg, P. L. Holland and T. D. Krauss, *Science*, 2012, **338**, 1321.
5 X. C. Wang, K. Maeda, A. Thomas, K. Takanabe, G. Xin, J. M. Carlsson, K. Domen and M. Antonietti, *Nat. Mater.*, 2009, **8**, 76.
6 K. Maeda and K. Domen, *J. Phys. Chem. Lett.*, 2010, **1**, 2655.
7 A. Kudo and Y. Miseki, *Chem. Soc. Rev.*, 2009, **38**, 253.
8 X. B. Chen, S. H. Shen, L. J. Guo and S. S. Mao, *Chem. Rev.*, 2010, **110**, 6503.
9 A. L. Linsebigler, G. Lu and J. T. Yates, Jr, *Chem. Rev.*, 1995, **95**, 735.
10 M. R. Hoffmann, S. T. Martin, W. Choi and D. W. Bahnemannt, *Chem. Rev.*, 1995, **95**, 69.
11 S. Rawalekar and T. Mokari, *Adv. Energy Mater.*, 2013, **3**, 12.
12 A. Kubacka, M. F. Garcia and G. Colón, *Chem. Rev.*, 2012, **112**, 1555.
13 P. V. Karmat, *J. Phys. Chem. Lett.*, 2012, **3**, 663.
14 H. Tada, T. Mitsui, T. Kiyonaga, T. Akita and K. Tanaka, *Nat. Mater.*, 2006, **5**, 782.
15 S. C. Hayden, N. K. Allam and M. A. El-Sayed, *J. Am. Chem. Soc.*, 2010, **132**, 14406.
16 J. Ryu, S. H. Lee, D. H. Nam and C. B. Park, *Adv. Mater.*, 2011, **23**, 1883.
17 D. R. Baker and P. V. Kamat, *Adv. Funct. Mater.*, 2009, **19**, 805.
18 H. Wang, G. Wang, Y. Ling, M. Lepert, C. Wang, J. Z. Zhang and Y. Li, *Nanoscale*, 2012, **4**, 1463.
19 Y. Chen, L. Wang, G. M. Lu, X. Yao and L. Guo, *J. Mater. Chem.*, 2011, **21**, 5134.
20 H. N. Kim, T. W. Kim, I. Y. Kim and S. J. Hwang, *Adv. Funct. Mater.*, 2011, **21**, 3111.
21 Y. Zhang, Y. Tang, X. Liu, Z. Dong, H. H. Hng, Z. Chen, T. C. Sum and X. Chen, *Small*, 2013, **9**, 996.
22 H. Tada, M. Fujishima and H. Kobayashi, *Chem. Soc. Rev.*, 2011, **40**, 4232.
23 C. Wang, R. L. Thompson, J. Baltrus and C. Matranga, *J. Phys. Chem. Lett.*, 2010, **1**, 48.
24 X. Chen and S. S. Mao, *Chem. Rev.*, 2007, **107**, 2891.
25 A. Fujishima, X. Zhang and D. A. Tryk, *Surf. Sci. Rep.*, 2008, **635**, 15.
26 H. G. Yang, C. H. Sun, S. Z. Qiao, J. Zou, G. Liu, S. C. Smith, H. M. Cheng and G. Q. Lu, *Nature*, 2008, **453**, 638.
27 C. T. Dinh, T. D. Nguyen, F. Kleitz and T. O. Do, *ACS Nano*, 2009, **3**, 3737.
28 C. T. Dinh, T. D. Nguyen, F. Kleitz and T. O. Do, *ACS Appl. Mater. Interfaces*, 2011, **3**, 2228.
29 C. B. Li, Z. J. Li, S. Yu, G. X. Wang, F. Wang, Q. Y. Meng, B. Chen, K. Feng, C. H. Tung and L. Z. Wu, *Energy Environ. Sci.*, 2013, **6**, 2597.
30 W. Zhu, X. Liu, H. Liu, D. Tong, J. Wang and J. Peng, *J. Am. Chem. Soc.*, 2010, **132**, 12619.
31 H. Park, W. Choi and M. R. Hoffmann, *J. Mater. Chem.*, 2008, **18**, 2379.
32 C. T. Dinh, Y. Seo, T. D. Nguyen, F. Kleitz and T. O. Do, *Angew. Chem., Int. Ed.*, 2012, **51**, 6608.
33 N. Bao, L. Shen, T. Takata and K. Domen, *Chem. Mater.*, 2008, **20**, 110.

 This journal is © The Royal Society of Chemistry 2014

Published on 28 January 2014. Downloaded by Université Laval on 15/05/2014 20:42:49.

34 Q. Li, B. Guo, J. Yu, J. Ran, B. Zhang, H. Yan and J. R. Gong, *J. Am. Chem. Soc.*, 2011, **133**, 10878.
35 X. Wang, G. Liu, L. Wang, Z. G. Chen, G. Q. M. Lu and H. M. Cheng, *Adv. Energy Mater.*, 2012, **2**, 42.
36 W. Wang, S. Liu, L. Nie, B. Cheng and J. Yu, *Phys. Chem. Chem. Phys.*, 2013, **15**, 12033.
37 Y. P. Yuan, S. W. Cao, L. S. Yin, L. Xu and C. Xue, *Int. J. Hydrogen Energy*, 2013, **38**, 7218.
38 G. Wang and Y. Li, *ChemCatChem*, 2013, **5**, 1294.
39 J. Ran, J. Yu and M. Jaroniec, *Green Chem.*, 2011, **13**, 2708.
40 J. Baran, M. Śledź, M. Drozd, A. Pietraszko, A. Haznar and H. Ratajczak, *J. Mol. Struct.*, 2000, **526**, 361.
41 *Zeta Potential of Colloids in Water and Waste Water*, ASTM Standard D 4187-82, American Society for Testing and Materials, 1985.
42 F. Kleitz, T. Czuryszkiewicz, L. A. Solovyov and M. Lindén, *Chem. Mater.*, 2006, **18**, 5070.
43 K. Zhang and L. Guo, *Catal. Sci. Technol.*, 2013, **3**, 1672.
44 L. Amirav and A. P. Alivisatos, *J. Phys. Chem. Lett.*, 2010, **1**, 1051.
45 K. Domen, J. N. Kondo, M. Hara and T. Takata, *Bull. Chem. Soc. Jpn.*, 2000, **73**, 1307.
46 J. Zhang, J. Yu, M. Jaroniec and J. R. Gong, *Nano Lett.*, 2012, **12**, 4584.
47 *Handbook of X-ray Photoelectron Spectroscopy*, ed. J. F. Moulder, W. F. Stickle, P. E. Sobol, K. D. Bomben and J. Chastain, Physical Electronics, Inc., Eden Prairie, MN, 1992.
48 M. C. Biesinger, B. P. Payne, L. W. M. Lau, A. Gerson and R. S. C. Smart, *Surf. Interface Anal.*, 2009, **41**, 324.
49 N. Sakai, Y. Ebina, K. Takada and T. Sasaki, *J. Am. Chem. Soc.*, 2004, **126**, 5851.
50 J. G. Yu, Y. Hai and B. Cheng, *J. Phys. Chem. C*, 2011, **115**, 4953.
51 A. J. Bard, R. Parsons and J. Jordan, *Standard Potentials in Aqueous Solution*, Marcel Dekker, New York, 1985.
52 M. C. Liu, L. Z. Wang, G. Q. Lu, X. D. Yao and L. J. Guo, *Energy Environ. Sci.*, 2011, **4**, 1372.